npj Materials Degradation

https://doi.org/10.1038/s41529-026-00772-1

Article in Press

Mechanistic investigation of hydrostatic pressure effects on stress corrosion cracking in Ti-6Al-4V welded joints

Received: 15 January 2026

Accepted: 8 March 2026

Cite this article as: Cui, Y., Liu, R., Liu, J. *et al.* Mechanistic investigation of hydrostatic pressure effects on stress corrosion cracking in Ti-6Al-4V welded joints. *npj Mater Degrad* (2026). https://doi.org/10.1038/s41529-026-00772-1

Yu Cui, Rui Liu, Jun Liu, Shuangyu Du, Wenquan Wang, Guo Jin, Peiling Ke, Fuhui Wang & Li Liu

Mechanistic investigation of hydrostatic pressure effects on stress corrosion cracking in Ti-6Al-4V welded joints

Yu Cui [1, 2], Rui Liu [3 *], Jun Liu [2, 3], Shuangyu Du [3], Wenquan Wang [4], Guo Jin [1], Peiling Ke [5], Fuhui Wang [3], Li Liu [3 *]

1 Institute of Surface/Interface Science and Technology, Key Laboratory of Superlight Material and Surface Technology of Ministry of Education, College of Material Science and Chemical Engineering, Harbin Engineering University, Harbin 150001, China

2 Shenyang National Laboratory for Materials Science, Institute of Metal Research, Chinese Academy of Sciences, Shenyang 110016, China

3 State Key Laboratory of Digital Steel, Northeastern University, Shenyang 110819, China

4 Beijing Aeronautical Technology Research Center, Beijing 100076, China

5 State Key Laboratory of Advanced Marine Materials, Ningbo Institute of Materials Technology and Engineering, Chinese Academy of Sciences, Ningbo, 315201, China

Abstract

The reliability of titanium alloy welded joints is critical to the service safety of deep-sea engineering systems. The welding thermal cycle generates complex microstructures in Ti-6Al-4V, resulting in pronounced mechanical and electrochemical heterogeneity across joint regions. Herein, in-situ electrochemical testing was conducted to investigate stress corrosion cracking (SCC)

* Corresponding author: Rui Liu and Li Liu. E-mail: liurui@mail.neu.edu.cn, liuli@mail.neu.edu.cn.

behavior in distinct weld zones under hydrostatic pressure. Results reveal that hydrostatic pressure accelerates electrochemical reactions and enhances the SCC susceptibility — most severely in the heat-affected zone. This heightened vulnerability stems from the transformed β phase and lamellar secondary α phase, which promotes strain localization and impairs repassivation capability. This work presents the evidence of region-dependent-SCC susceptibility in Ti-6Al-4V welds under hydrostatic pressure, offering essential experimental insights for the safety assessment and welding optimization in deep-sea titanium structures.

Introduction

Deep-sea engineering equipment is trending toward larger scale, greater diving depth, and extended service life. Titanium alloys have become key materials for manufacturing pressure-resistant structures, piping systems, and exploration devices due to their exceptional specific strength and outstanding corrosion resistance. As an indispensable manufacturing process for large-scale titanium alloy components, welding plays a critical role in ensuring the structural integrity and operational safety of the entire system. Common welding techniques for titanium alloys include tungsten inert gas welding (TIG), gas metal arc welding (GMAW), plasma arc welding (PAW), laser beam welding (LBW), and electron beam welding (EBW) [1]. Because titanium alloys are highly susceptible to hydrogen embrittlement, air containing water vapor should be avoided during welding. TIG welding, with its high energy density and good weld quality, is widely used for joining medium-thick titanium alloy plates [2, 3].

During the welding of α+β titanium alloys, the thermal cycle leads to complex microstructures

in both the weld metal (WM) and the heat-affected zone (HAZ). For instance, in Ti-6Al-4V, the high undercooling in the weld center promotes the formation of an interlaced basket-weave structure composed of acicular α′ martensite, while the HAZ exhibits a gradient microstructure—ranging from fine α′ martensite adjacent to the fusion line to transformed β phase and alternating α/α′ lamellar structures adjacent to the base metal (BM) [4]. This microstructural complexity results in significant mechanical property differences between the welded regions and the base material. For example, the Widmanstätten structure in the HAZ contains coarse acicular α phases that act as crack initiation sites under stress; moreover, the softer β phase between α needles cannot effectively transfer load, thereby reducing the joint strength. In contrast, the basket-weave microstructure in the WM, with its uniformly interwoven α+β phases, enables efficient load transfer and can withstand higher stresses [5].

Beyond mechanical effects, microstructural complexity also influences electrochemical corrosion behavior. For instance, the columnar grain structure in the WM is more prone to solute segregation at grain boundaries compared to equiaxed grains, leading to interfacial potential differences [6]. Additionally, the presence of metastable α′ martensite in LBW-welded Ti-6Al-4V joints results in inferior corrosion resistance compared to the BM [7-9]. Other factors such as grain size, local strain, β/α phase ratio, and high-angle grain boundaries also significantly affect the corrosion resistance of titanium alloy welded joints [10, 11]. Consequently, the combined mechanical and electrochemical heterogeneity leads to region-dependent SCC behavior in corrosive environments. Zhang et al. [12] simulated various titanium alloy weld microstructures via heat treatment and found that the Widmanstätten structure in the HAZ exhibits poor resistance

to SCC. Similarly, Gao et al. [13] measured the critical stress intensity factor for SCC (K_{1SCC}) in different regions of Ti-6321 welded joints and reported that the HAZ has the lowest K_{1SCC}, making it most prone to SCC.

Hydrostatic pressure is a defining characteristic of deep-sea environments. Numerous studies have demonstrated its significant impact on the corrosion resistance and SCC susceptibility of alloys [14-18]. Hydrostatic pressure alters the distribution of metal ions at the metal/solution interface, reduces the thickness of the Helmholtz layer (amplifying the ψ_1 effect), and modifies the partial molar volume of interfacial species, thereby accelerating electrochemical corrosion reactions [19, 20]. Consequently, it enhances galvanic corrosion between dissimilar alloys or microstructural phases [21, 22]. As a typical α+β titanium alloy, Ti-6Al-4V exhibits increased SCC tendency under high hydrostatic pressure due to accelerated dissolution of the β phase and the formation of an unstable passive film under coupled stress and pressure, as reported by Liu et al. [23-25]. Pan et al. found that high pressure promotes crack propagation, Cl^- enrichment, hydrogen penetration, and passive film rupture, which drives the SCC process and results in high crack propagation rate by studying the stress corrosion behavior of Ti-6Al-3Nb-2Zr-1Mo welded joints under different environments[26, 27].

Despite progress in understanding the stress corrosion behavior of titanium alloys, the specific interplay between hydrostatic pressure and microstructural heterogeneity in welded joints remains largely unexplored. Most studies to date have focused on individual regions under atmospheric pressure, offering limited insight into the synergistic effects of hydrostatic pressure and weld microstructure under realistic deep-sea conditions. To address this gap, the present work combines

in-situ electrochemical measurements with EBSD analysis to systematically evaluate the SCC behavior of the HAZ, WM, and BM in Ti-6Al-4V welded joints subjected to varying hydrostatic pressures. The results identify the HAZ as the most susceptible region, with hydrostatic pressure markedly increasing its SCC susceptibility. These findings offer a foundation for assessing the reliability of deep-sea titanium welded structures and guide the optimization of welding processes for extreme environments.

Results and discussion

Mechanical properties of welded titanium alloy joints

The engineering stress-strain curves of Ti-6Al-4V welded joints tested by slow strain rate (SSRT) in air, under 0.1 MPa and 15 MPa in NaCl solution, are shown in Fig. 1. There are significant differences in the tensile results among the three different zones, with the mechanical properties of the BM being significantly superior to those of the HAZ and WM. Hydrostatic pressure does not alter the deformation behavior during the elastic stage but significantly reduces the fracture elongation and strength. Fig. 2 shows the measured results of yield strength, fracture strength, fracture elongation, and I_{SSRT} after SSRT, respectively. The BM exhibits the highest yield and tensile strengths in air, 0.1 MPa, and 15 MPa conditions; whereas the yield and tensile strengths of the HAZ and WM are also markedly lower. Both NaCl solution and hydrostatic pressure reduce the strength of titanium alloy welded joints. Specifically, for the BM, the yield and tensile strengths decreased from about 910 MPa and 965 MPa in air to about 860 MPa and 905 MPa in the 15 MPa pressurized solution, respectively. For the HAZ, the yield and tensile strengths

decreased from about 825 MPa and 860 MPa in air to about 780 MPa and 825 MPa in the 15 MPa pressurized solution, respectively. Additionally, the BM shows the best average fracture elongation in air, 0.1 MPa, and 15 MPa saline solutions, at 15.6%, 14.9%, and 14.3%, respectively. Both the ductility of the HAZ and WM are significantly lower than that of the BM, with the average elongation of HAZ in three environments being only 11.3%, 10.0%, and 9.4%, respectively. Calculating the I_{SSRT} of different welding zones of titanium alloys (Fig. 2(d)), it can be seen that with the increase of hydrostatic pressure, I_{SSRT} increases to varying degrees. The BM has the lowest I_{SSRT} under 0.1 MPa and 15 MPa hydrostatic pressures, at 0.10 and 0.16, respectively, while the HAZ exhibits the strongest sensitivity under 0.1 MPa and 15 MPa hydrostatic pressures, with I_{SSRT} increasing to 0.13 and 0.20. This suggests that the higher β-transformed phase content and unique platelike α phase in the HAZ may be critical factors contributing to the reduced mechanical properties and increased stress corrosion susceptibility of the weld region.

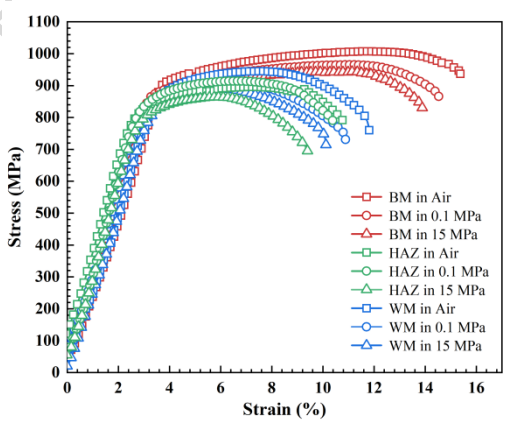

Fig. 1 Stress-strain curves of Ti-6Al-4V for different welding regions.

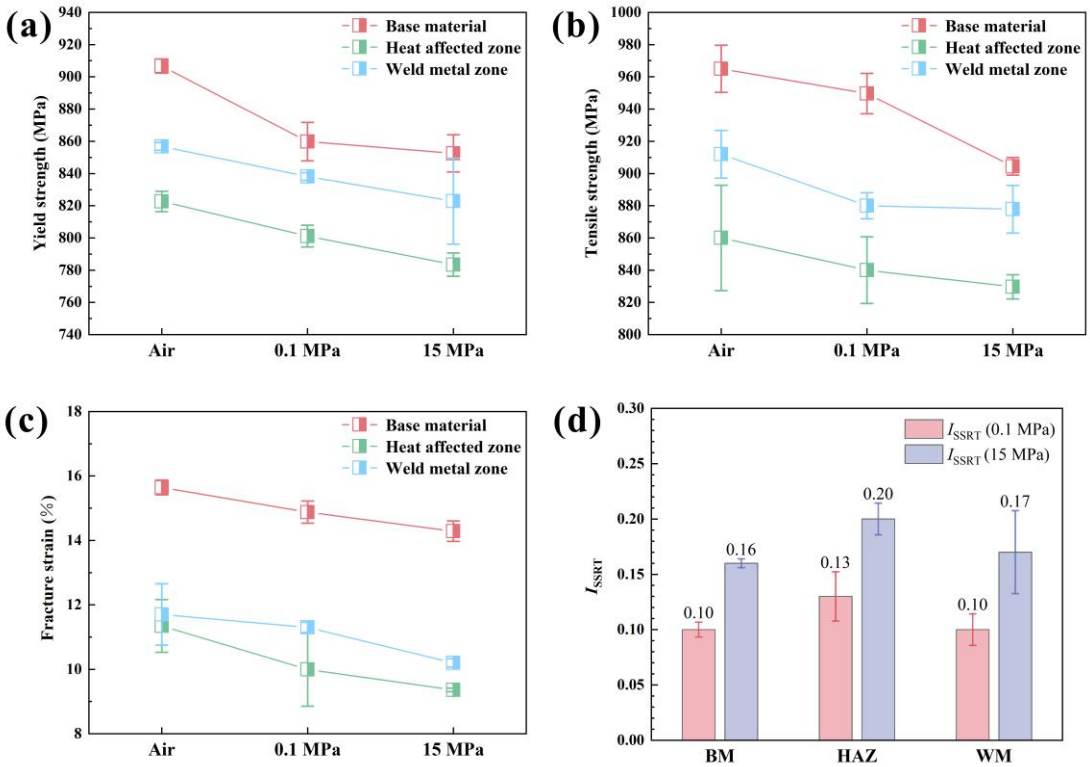

Fig. 2 Mechanical properties of Ti-6Al-4V as determined by SSRT. (a) Yield strength, (b) ultimate tensile strength, (c) fracture elongation, and (d) stress corrosion cracking susceptibility.

Morphologies of welded titanium alloy joints

The fracture surface morphologies following SSRT are shown in Figs. 3~5. Secondary cracks were observed on the macroscopic fracture surfaces of all three regions. The BM samples predominantly exhibited fibrous fracture features, characterized by numerous uniformly distributed dimples with fine pores at their base, indicative of ductile fracture. In NaCl solution, the dimples in the BM samples became elongated and were accompanied by tearing features (Figs. 3(b-c)). Additionally, the BM samples fractured under 15 MPa hydrostatic pressure exhibited distinct river-like quasi-cleavage patterns (red-marked area in Fig. 3(c)), with slip traces visible on the cleavage planes (dashed-line marked area in Fig. 3(c)). Compared to the BM, the HAZ and

WM samples exhibited shallower dimple morphologies in air and ambient pressure NaCl solution (Figs. 4~5), indicating poorer ductility. Under 15 MPa hydrostatic pressure, large areas of quasi-cleavage structure were observed (red-marked areas in Figs. 4~5), with smooth cleavage planes and shallow, less noticeable slip traces.

To quantitatively assess the effect of environmental conditions on fracture behavior, the fractal dimensions of the fracture surfaces were determined using the fracture profile method, which captures the tortuosity of the crack propagation path. In Fig. 6, hydrostatic pressure reduced the fractal dimension of the dimple-fiber regions, with the most significant reduction occurring in the HAZ. This decrease in fractal dimension directly reflects a straightening of the crack path, consistent with the microstructural observations in Figs. 3~5, namely, shallower dimples, increased cleavage facets, and reduced slip trace definition. A straighter crack propagation path implies lower energy dissipation during fracture and diminished resistance to crack growth.

This embrittlement tendency observed in the fracture surfaces can be traced back to the distinct deformation behaviors of the different zones under hydrostatic pressure. As shown in Fig. S2, under 0.1 MPa, the WM accommodated strain via single slip, characterized by parallel slip lines within grains. Under 15 MPa, however, the WM exhibited orthogonal slip lines indicative of multiple slip activation and severe localized deformation. This transition arises from strain partitioning: the HAZ, which showed significantly less deformation under 15 MPa, failed to accommodate the overall strain, forcing the WM to bear a larger portion of the plastic strain. The resulting intense multi-slip prematurely consumed ductility and introduced local damage in the WM, facilitating crack propagation and contributing to the flattened fracture surface. Meanwhile,

the minimal deformation in the HAZ under high pressure suggests that its microstructure (e.g., β-transformed and plate-like secondary α phases) becomes inherently less deformable, making it more susceptible to brittle fracture once cracking initiates. The observed trends in ductility and strength loss correlate well with the changes in fractal dimension, further confirming that high-pressure environments promote embrittlement in the titanium alloy. The HAZ demonstrates the highest susceptibility to this effect, identifying it as the most vulnerable region for deep-sea applications of this material.

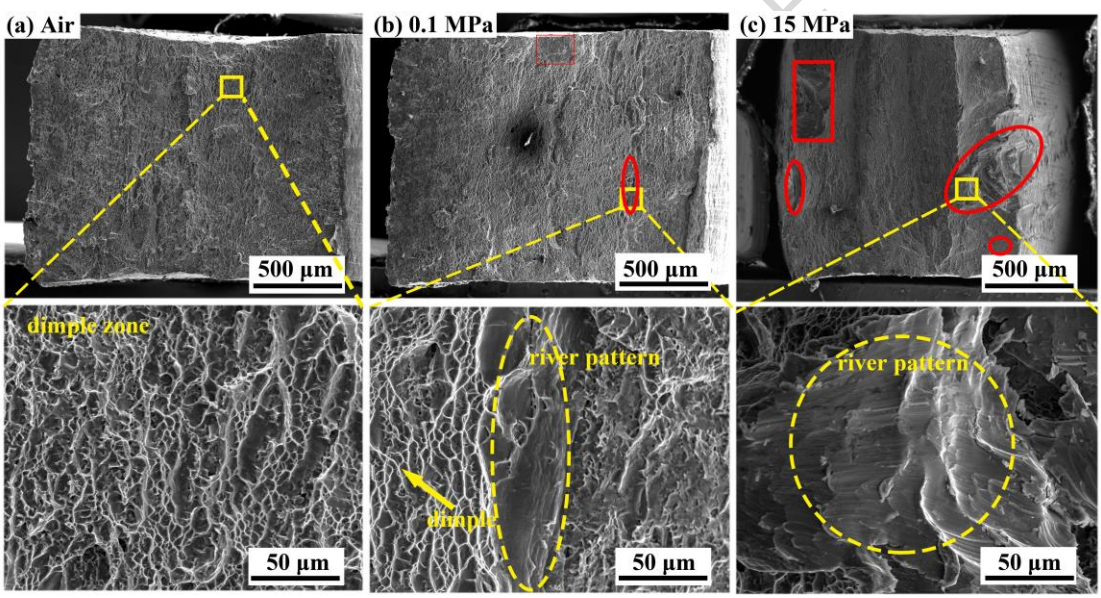

Fig. 3 Fracture morphology of BM samples post SSRT. (a) In air, (b) in 3.5% NaCl solution at 0.1 MPa, and (c) in 3.5% NaCl solution at 15 MPa.

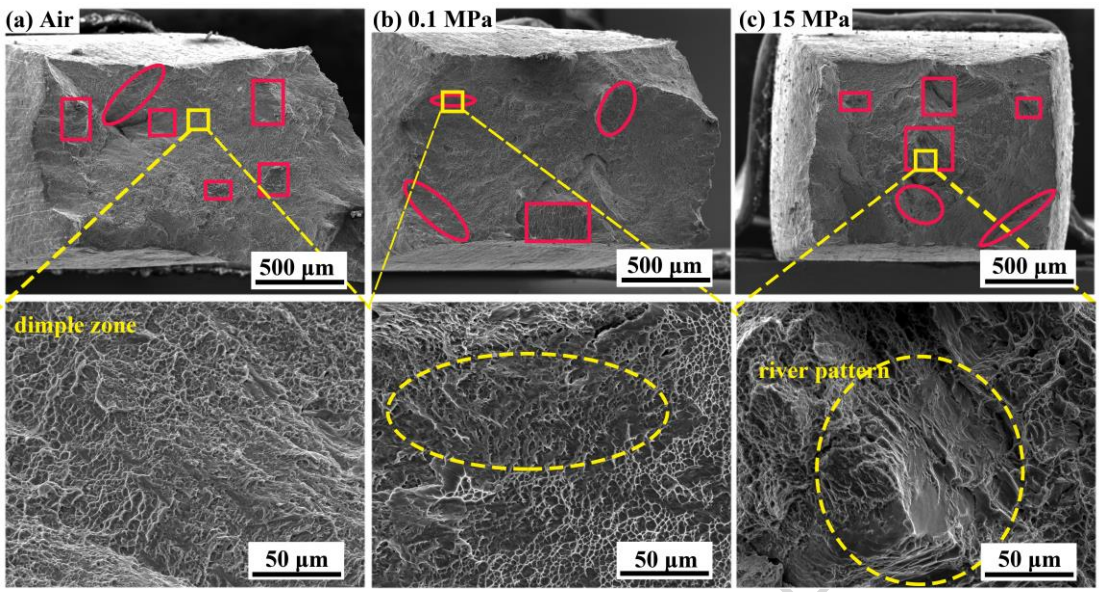

Fig. 4 Fracture morphology of HAZ samples post SSRT. (a) In air, (b) in 3.5% NaCl solution at 0.1 MPa, and (c) in 3.5% NaCl solution at 15 MPa.

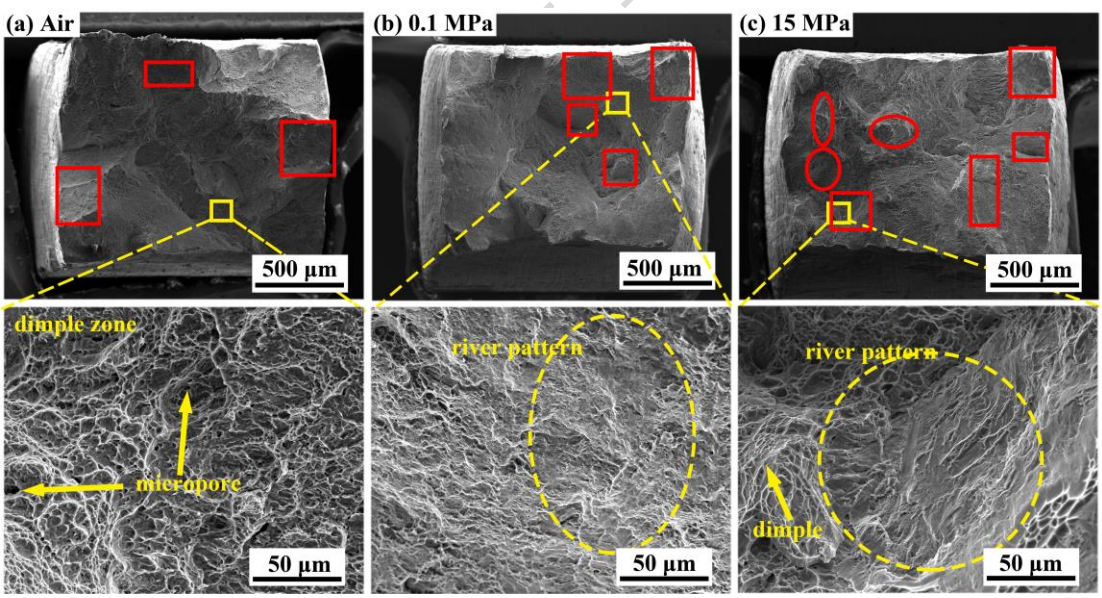

Fig. 5 Fracture morphology of WM samples post SSRT. (a) In air, (b) in 3.5% NaCl solution at 0.1 MPa, and (c) in 3.5% NaCl solution at 15 MPa.

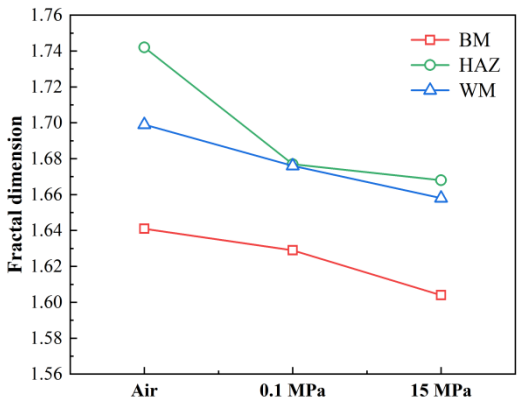

Fig. 6 Analysis of fractal dimension on dimple areas of tensile fracture surfaces of Ti-6Al-4V weld specimens under different environmental conditions.

Inverse pole figure (IPF) maps (Figs. 7~8) reveal that the initial state of the BM contains abundant equiaxed α phases within macro-zones. Upon SSRT tests to yield under 15 MPa hydrostatic pressure, these macro-zones elongated, forming pronounced {0001} basal textures. In contrast, the platelike α and α′ phases in the HAZ and WM did not develop significant textures or experience weakened texture intensity under high hydrostatic pressure (Figs. 8(b-c)). This difference is attributed to the larger grain size and specific slip systems such as {10-10}<11-20> and {10-11}<11-23> in the BM [28], which facilitates c-axis alignment during deformation. Kernel Average Misorientation (KAM) images indicate local orientation variations (Figs. 9(a-b)). Before tensile testing, the BM exhibited the highest average local misorientation, allowing uniform strain distribution outside macro-zones. The HAZ showed the lowest average local misorientation but contained elongated bands with high local misorientations spanning multiple platelike secondary α phases, representing early shear bands dominated by dislocation slip. Furthermore, some strain concentration was also observed in the β-transformed phase.

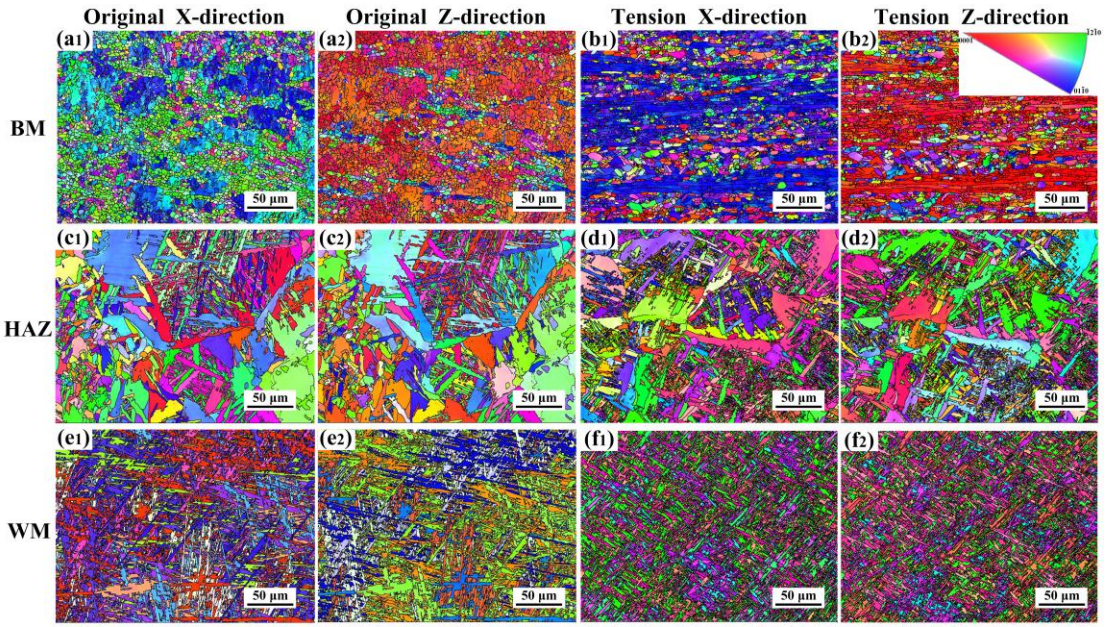

Fig. 7 Orientation maps of different welding zones in Ti-6Al-4V. (a1, a2) Orientation maps in the x-direction and z-direction of the original BM samples, (b1, b2) orientation maps in the x-direction and z-direction of BM samples after SSRT to yield under 15 MPa, (c1, c2) orientation maps in the x-direction and z-direction of the original HAZ samples, (d1, d2) orientation maps in the x-direction and z-direction of HAZ samples after SSRT to yield under 15 MPa, (e1, e2) orientation maps in the x-direction and z-direction of the original WM samples, and (f1, f2) orientation maps in the x-direction and z-direction of WM samples after SSRT to yield under 15 MPa.

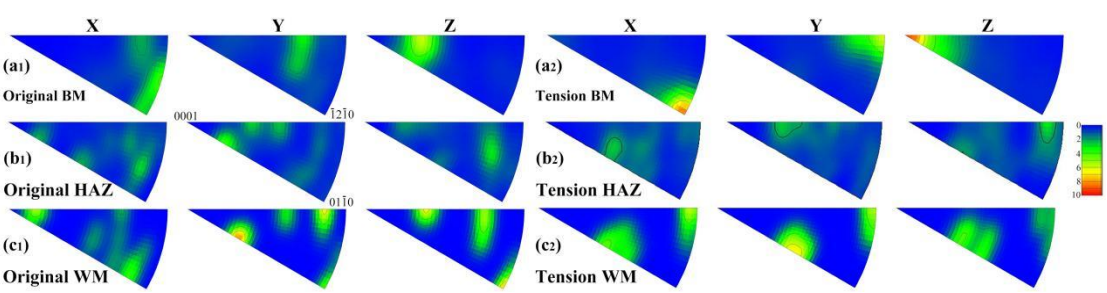

Fig. 8 IPF maps of different welding regions in Ti-6Al-4V. (a1) IPF map of the original BM samples, (a2) IPF map of BM samples after SSRT to yield under 15 MPa, (b1) IPF map of the original HAZ samples, (b2) IPF

map of HAZ samples after SSRT to yield under 15 MPa, (c1) IPF map of the original WM samples, and (c2) IPF map of WM samples after SSRT to yield under 15 MPa.

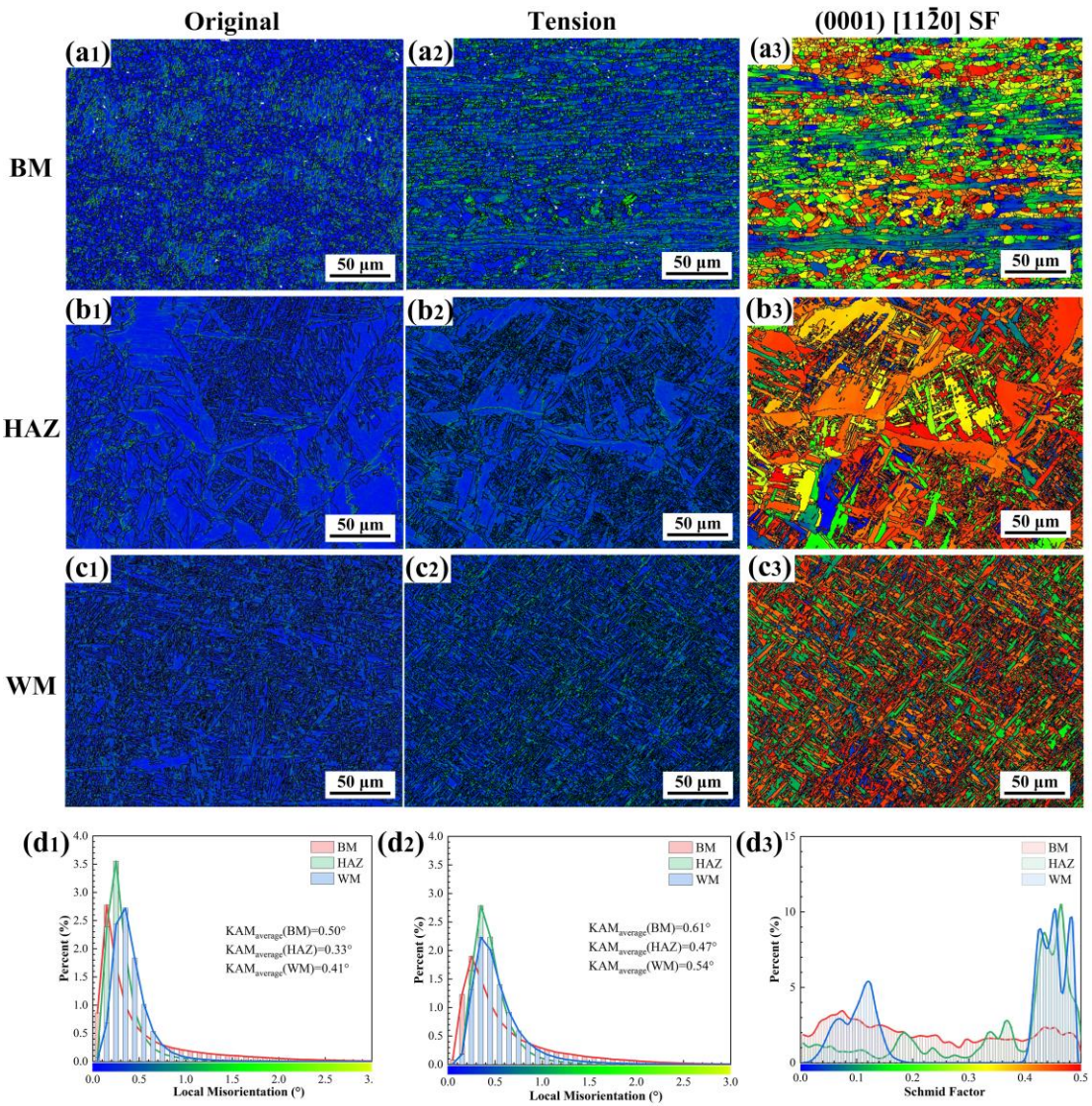

Fig. 9 KAM and basal slip Schmid factor maps of different welding zones in Ti-6Al-4V. (a1) KAM map of the original BM samples, (a2, a3) KAM map and basal slip Schmidt factor map of BM samples after SSRT to yield under 15 MPa, (b1) KAM map of the original HAZ samples, (b2, b3) KAM map and basal slip Schmid factor map of HAZ samples after SSRT to yield under 15 MPa, (c1) KAM map of the original WM samples, (c2, c3) KAM map and basal slip Schmid factor map of WM samples after SSRT to yield under 15 MPa, (d1) Distribution

of original local misorientation across different welding zones, and (d2, d3) distribution of local misorientation and basal slip Schmid factor across different welding zones after SSRT to yield under 15 MPa.

After SSRT under 15 MPa hydrostatic pressure, the average local misorientation increased for all three regions. Specifically, the BM samples showed significant strain concentration within soft-oriented grains in non-macro-zones (see Schmid factor maps, Fig. 9(c)). In the Schmid factor maps, the (0001) slip plane is parallel to the tensile direction, while the [11-20] slip direction is perpendicular to the tensile direction. During yielding, soft grains around hard-oriented grains in the BM preferentially yielded and bore most of the strain, while macro-zones formed {0001} basal textures, acting as hard grains maintaining overall alloy strength through stress concentration and dislocation hindrance, thus preserving better yield strength under high hydrostatic pressure. Conversely, the HAZ and WM samples exhibited significantly lower yield strengths under 15 MPa. This is attributed to the generally higher Schmid factors in these regions, which result in larger resolved shear stresses on the slip systems under applied loading, thereby facilitating easier slip initiation and plastic deformation. Moreover, for the HAZ samples deformed under high pressure, the strain concentration bands in platelike secondary α phases were notably extended and increased, indicating that high hydrostatic pressure further disrupted strain uniformity in the HAZ, leading to a substantial reduction in mechanical properties under high-pressure environments.

Electrochemical properties of welded titanium alloy joints

Continuous EIS measurements were performed on the different zones of the titanium alloy welded joints in NaCl solution under 0.1 MPa and 15 MPa hydrostatic pressures to evaluate the growth of passive films. Nyquist plots primarily exhibited semicircular shapes (Fig. 10), while

Bode plots (Fig. S1) showed broad single peaks or overlapping double peaks. These results indicated two-time constants in the EIS spectra across different welding regions under both hydrostatic pressures. During continuous measurements, the diameter of the capacitive arc representing the passive film increased over time, indicating spontaneous and continuous passive film growth on the titanium surface. Compared to ambient conditions, the growth rate of the capacitive arc radius under 15 MPa hydrostatic pressure was much slower and smaller. Notably, the HAZ exhibited the smallest capacitive arcs among the three regions under both pressures.

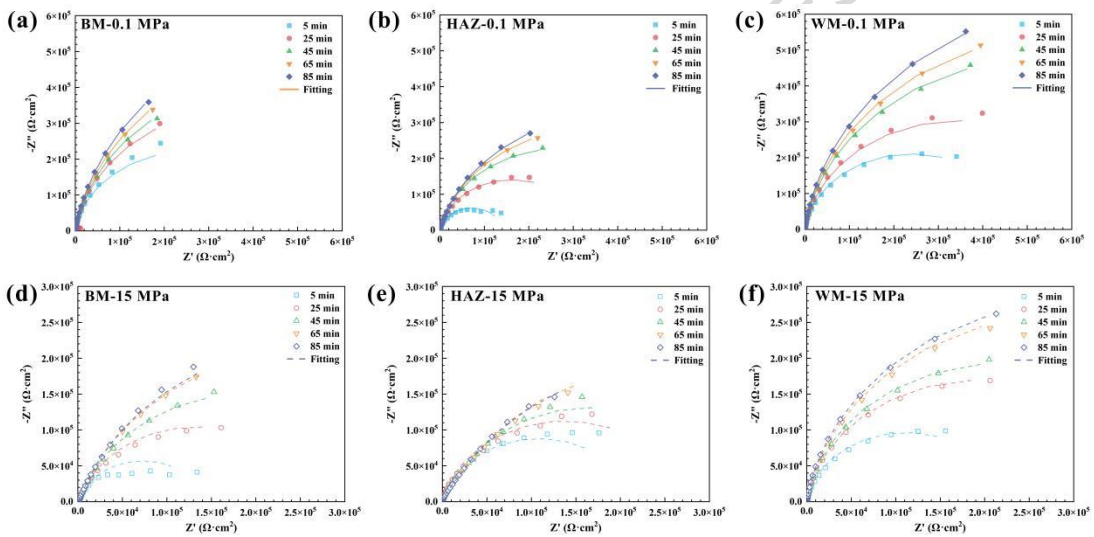

Fig. 10 EIS results of different welding regions of Ti-6Al-4V. (a) Nyquist plot of BM samples in solution at 0.1 MPa, (b) Nyquist plot of HAZ samples in solution at 0.1 MPa, (c) Nyquist plot of WM samples in solution at 0.1 MPa, (d) Nyquist plot of BM samples in solution at 15 MPa, (e) Nyquist plot of HAZ samples in solution at 15 MPa, and (f) Nyquist plot of WM samples in solution at 15 MPa.

Considering that the EIS data were obtained after removing the surface passive film formed in air, they reflect the formation process of the passive film on fresh titanium surfaces. An equivalent circuit (EC) with two-time constants was used to describe the passive film growth (Fig.

11(a)) [17, 29]. R_s represents the solution resistance, and constant phase element (CPE) replaces ideal capacitance due to surface dielectric heterogeneity. CPE_1 and R_1 describe charge transfer within the passive film, while CPE_{dl} and R_{ct} represent the double-layer capacitance at the passive film/solution interface and metal substrate/solution interface. The equivalent capacitance of CPE can be calculated using $C_{eff}=Q^{1/n}R^{(1-n)/n}$ [30], where Q and n are CPE fitting parameters, and R is the parallel resistance. The fitting curve of Fig. 10 is in good agreement with the experimental data. The fitting results are shown in Table S1, and the chi-square coefficient (χ^2) is from 10^{-4} to 10^{-3}. Fig. 11(b) shows the variation of fitting parameter R_1, which reflects the compactness of the passive film. During the immersion period from 5 min to 45 min in an atmospheric environment, the R_1 average values of the BM and WM regions at 0.1 MPa were similar, increasing from 5.1×10^5 $\Omega \cdot cm^2$ to 1.5×10^6 $\Omega \cdot cm^2$; whereas the HAZ had the smallest R_1 value, only increasing from 1.9×10^5 $\Omega \cdot cm^2$ to 6.8×10^5 $\Omega \cdot cm^2$. Under a hydrostatic pressure of 15 MPa, the growth rate of R_1 for the HAZ noticeably slowed down, with R_1 increasing slowly from 1.6×10^5 $\Omega \cdot cm^2$ to 4.2×10^5 $\Omega \cdot cm^2$, being the slowest among the three welding microstructures.

Meanwhile, Fig. 11(c) plots the change curve of the average value of $1/C_{eff,1}$ (which is proportional to the thickness of the passive film) over time. For the BM and WM regions, $1/C_{eff,1}$ increases linearly with ln(t), indicating that the growth of the passive film in these regions aligns with the point defect model [31-33], governed by the inward transport of oxygen vacancies within the film. Under 15 MPa, the slope of the $1/C_{eff,1}$-ln$t$ curve for BM and WM is lower, reflecting that hydrostatic pressure inhibits the growth process of the passive film on titanium alloy surfaces. In contrast, the $1/C_{eff,1}$ of the HAZ decreases gradually over time, showing a poor linear relationship

with ln(t), suggesting signs of destabilization in the passive film of the HAZ, influenced by anion injection at the interface, leading to a dissolution trend.

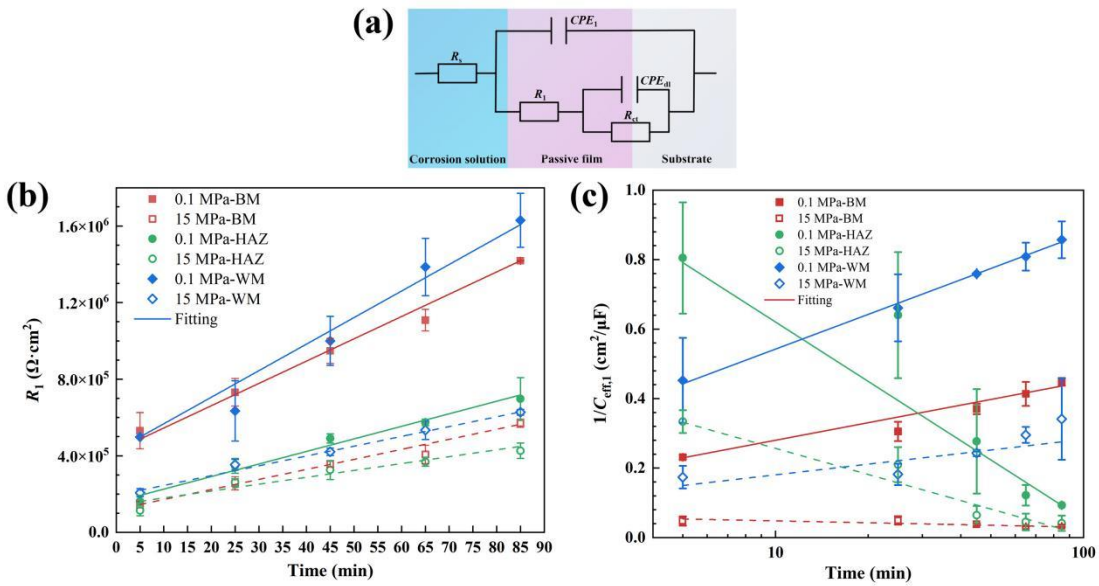

Fig. 11 Fitting results of electrochemical impedance of different welding regions. (a) Equivalent circuit, (b) variation pattern of fitting parameter R_1, and (c) variation pattern of fitting parameter $1/C_{eff,1}$.

For passive metals, the rupture of the passive film is the first step in stress corrosion cracking[34], followed by dissolution and hydrolysis reactions that lead to acidification of the solution environment at the site of the passive film rupture and at the crack tip[35]. Qiao et al.[36, 37] found in their studies that corrosion processes at the metal/passive film interface cause deformation, generating additional stresses, which further exacerbate the rupture of the passive film due to corrosion-induced external stresses. Regardless of whether the passive film rupture is caused by the corrosion process or external stresses, it becomes the site for the initiation of micro-cracks. When a large number of slip steps appear on the metal surface, the unprotected metal matrix will be exposed to the corrosive medium. At this point, due to the action of aggressive ions, the

bare metal does not undergo sufficient repassivation immediately, i.e., a complete passive film structure is not formed instantly, which also explains why the I_{SSRT} in the HAZ region is the highest in the solution environment, reaching up to 20% under high hydrostatic pressure conditions.

The stress corrosion mechanism of different welded regions in Ti-6Al-4V alloy under a hydrostatic pressure of 15 MPa is illustrated in Fig. 12. It can be seen that the increased stress corrosion susceptibility of titanium alloy welded joints mainly results from the combined effect of the material's intrinsic microstructure and the high hydrostatic pressure environment. In the HAZ, the presence of large amounts of β-transformed phases, plate-like secondary α phases, and fine martensitic α′ phases leads to microstructural inhomogeneity, significantly extending and increasing the number of strain localization bands, thereby disrupting strain uniformity. Under high hydrostatic pressure, the passive film in the HAZ becomes unstable and exhibits the poorest repassivation capability. Once the passive film ruptures, the exposed bare HAZ is subjected to the corrosive medium. The HAZ is unable to rapidly form a complete passive film, causing the fracture behavior of the titanium alloy to shift from ductile to brittle, which has the most pronounced effect on the HAZ and further exacerbates its susceptibility to stress corrosion.

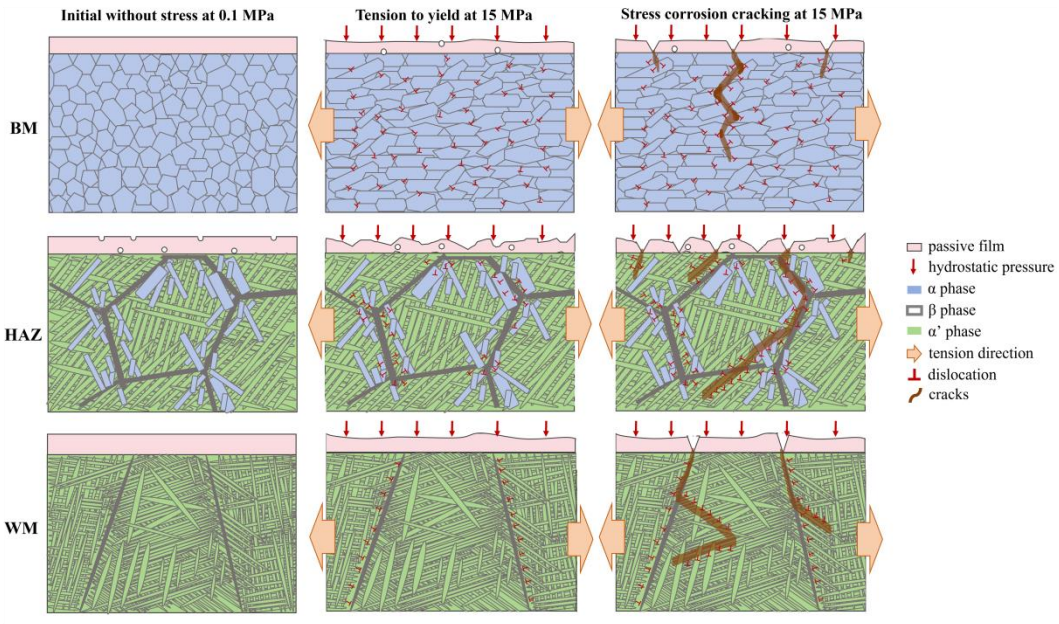

Fig. 12 The schematic diagram of stress corrosion mechanism of Ti-6Al-4V alloy in different welding areas under 15 MPa hydrostatic pressure

In summary, this study provides fundamental insights into the stress corrosion behavior of titanium alloy welded joints under hydrostatic pressure. Specifically, the heat-affected zone (HAZ) exhibits markedly reduced deformability in high-pressure environments, which forces the weld metal (WM) to accommodate excessive local strain through multi-slip activation. This pressure-induced transition from single to multiple slip systems prematurely exhausts the ductility of the WM and facilitates crack initiation, ultimately manifesting as a flattened fracture morphology. The inherent vulnerability of the HAZ stems from its microstructural constituents (β-transformed and plate-like secondary α phases), which limit its deformability under pressure and render it prone to brittle fracture upon crack onset. Alongside this mechanical perspective, electrochemical analysis reveals that hydrostatic pressure suppresses repassivation in the HAZ, compromising passive film stability. The synergy between strain concentration in the WM and film instability in the HAZ

underpins the enhanced stress corrosion susceptibility of the HAZ relative to the other weld zones. These findings establish that environmental embrittlement under deep-sea conditions arises from a coupled mechanism involving both strain redistribution across microstructural zones and localized degradation of passive film stability, providing a mechanistic basis for improving the reliability of welded titanium components in deep-sea applications.

Methods

Materials and welding procedure

Ti-6Al-4V alloy thick plates were used as the base material, and matching filler wire of the same alloy was employed. Prior to welding, the plates were degreased using deionized water and ethanol. A TIG process was then performed. The final welded plate dimensions were 300 mm × 150 mm × 15 mm, with a weld pool width of 15 mm (Fig. 13(a)) and a weld shape factor of 1.0. Welding parameters are listed in Table 1. The PAW process induced significant microstructural evolution, resulting in a joint composed of three distinct regions: the HAZ, WM, and unaffected BM, as shown in optical micrographs (Figs. 13(d-h)). Due to varying thermal cycles experienced from the weld center to the base material, each region developed a unique microstructure, the difference in microstructure can be explained by the CCT phase diagram in Fig. 13(c). It can be clearly seen from the CCT diagram that the critical cooling rate for the formation of complete martensitic α′ phase is 410 °C/s, which corresponds to the WM at the center of the molten pool. When the cooling rate is lower than 20 °C/s, only Widmanstatten α and primary α and β phases

are formed, which is the BM region of the forged sheet that is not affected by the thermal cycle. The HAZ is between the cooling rates of 410 ~ 20 °C/s, and the β phase is partially transformed into the α′ phase, accompanied by a large block of α phase. The BM (Fig. 13(d)) consists primarily of equiaxed α phase with intergranular β phase; the WM center (Fig. 13(f)), subjected to temperatures well above the melting point and rapid cooling, formed acicular α′ martensite; the narrow transitional HAZ exhibits a microstructural gradient—from equiaxed a and transformed β near the BM (Fig. 13(g)), through primary a with lamellar transformed β containing secondary α (Fig. 13(e)), to fine acicular α/α′ and retained primary β adjacent to the WM (Fig. 13(h)).

Table 1 TIG welding parameters for Ti-6Al-4V alloys.

Welding Parameters	Values
Welding current (A)	200
Welding voltage (V)	17
Welding speed (cm/min)	15
Plasma gas flow rate (lpm)	5
Torch position	Vertical

Slow strain rate testing (SSRT)

To investigate SCC under hydrostatic pressure, tensile specimens were cut from the welded plate via electrical discharge machining (EDM) according to ASTM G129 [38], with the gauge section positioned within the BM, HAZ, or WM (Fig. 13(a)). Specimen geometry is shown in Fig. 13(b). SSRT tests were conducted using a deep-sea environment simulation system (Bairoe, Shanghai) at a strain rate of 10^{-5} s^{-1} in three environments: air, 0.1 MPa hydrostatic pressure + 3.5 wt.% NaCl solution, and 15 MPa hydrostatic pressure + 3.5 wt.% NaCl solution. Engineering

stress–strain curves were recorded via a data acquisition system. The SCC susceptibility was quantified using the SSRT index (I_{SSRT}), calculated as [39]:

$$I_{SSRT}=1-\frac{[\sigma_{sol}\times(1+\delta_{sol})]}{[\sigma_{air}\times(1+\delta_{air})]} \quad (1)$$

where δ_{air} and δ_{sol} are the elongations to fracture in air and solution, respectively, and σ_{air} and σ_{sol} are the corresponding ultimate tensile strengths. I_{SSRT} ranges from 0 (no susceptibility) to 1 (extreme susceptibility). All tests were repeated at least three times, and average values were reported.

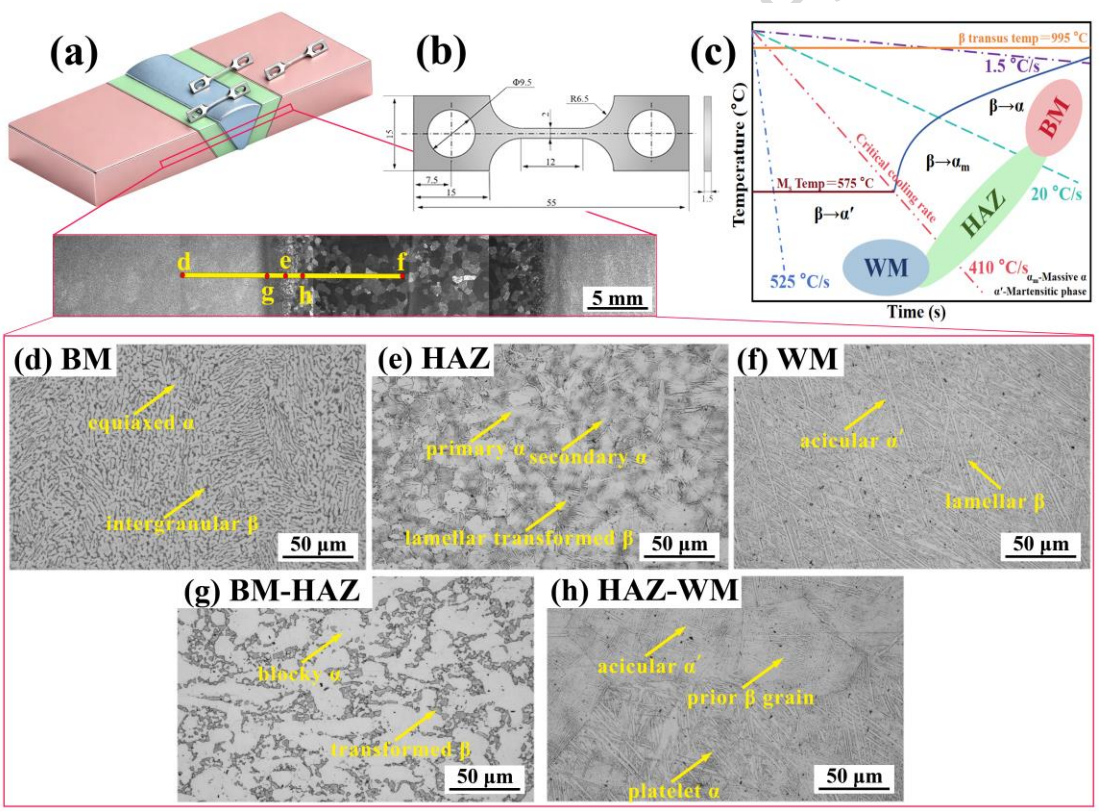

Fig. 13 Schematic representation and microstructural analysis of titanium alloy welding. (a) Sampling diagram of a Ti-6Al-4V welded plate, (b) dimensions of tensile specimens, (c) CCT phase diagram of Ti-6Al-4V alloy[40, 41], (d) metallographic microscope image of BM, (e) metallographic microscope image of HAZ, (f)

metallographic microscope image of WM, (g) metallographic microscope image of HAZ adjacent to BM, and (h) metallographic microscope image of HAZ near WM.

Microstructural characterization

All specimens were ground progressively with SiC papers from 240# to 2000#, then cleaned sequentially with deionized water, acetone, and ethanol, and dried with cold air. For optical microscopy (Axio Observer Z1, Zeiss), specimens were mechanically polished and etched in a solution of 2 vol.% HF + 8 vol.% HNO_3 to reveal microstructures. Fracture surfaces from SSRT tests in air, 0.1 MPa NaCl solution, and 15 MPa NaCl solution were examined using a field-emission SEM (INSPECT F50, FEI) in secondary electron mode. Fractal dimension analysis was employed to quantify fracture surface roughness. After grayscale conversion and filtering, the Marr–Hildreth algorithm was used to detect dimple edges, and the box-counting method was applied to calculate the fractal dimension. EBSD was performed on as-welded samples and on samples tensile-tested to yield under 15 MPa hydrostatic pressure. EBSD specimens were electropolished in a solution of 10 vol.% perchloric acid + 90 vol.% ethanol at −30 °C.

Electrochemical Measurements

All electrochemical tests were conducted using an Autolab integrated with a high-pressure autoclave simulating deep-sea conditions. A standard three-electrode cell was used: the specimen as the working electrode, an Ag/AgCl (1 mol/L KCl) reference electrode rated for high pressure, and a platinum mesh counter electrode. According to ASTM G30 [42], 0.5 mm-thick Ti-6Al-4V welded sheets were bent into U-shaped specimens with a 5 mm radius. The specimens were connected to copper wires and sealed with epoxy resin, exposing only ~1 cm^2 of the top surface

(corresponding to BM, HAZ, or WM). Tests were performed at room temperature in 3.5 wt.% NaCl solution under hydrostatic pressures of 0.1 MPa and 15 MPa. Prior to testing, all specimens were potentiostatically polarized at −1.5 V (vs. Ag/AgCl) for 2 min to remove native or pre-formed surface oxides. After open-circuit potential (OCP) stabilization, five consecutive electrochemical impedance spectroscopy (EIS) measurements were performed to assess passive film growth. EIS used a 10 mV sinusoidal perturbation over a frequency range of 10^5 to 10^{-2} Hz.

Data availability

The data supporting the main findings are available in the manuscript and supplementary information file. Additional support can be obtained from the corresponding author upon reasonable request.

Declarations

Funding

This work was financially supported by the National Natural Science Foundation of China (U22A20111, U24A2030) and the Opening Project of Key Laboratory of Advanced Marine Materials (2024K06).

Acknowledgements

Not applicable.

Author contributions

Y. C. (first author): wrote the original draft and maintained the equipment used in this work. R. L. (corresponding author): reviewed and edited the manuscript, conceptualization and design of

the experimental protocols. J. L. and S. D.: investigation, formal analysis, and wrote the original draft. W. W. and G. J.: signing experimental protocols. L. L.: designing experimental protocols. K. P. and F.W.: funding acquisition and provided research materials, samples, and instruments.

All authors read and approved the final version.

Competing Interests

Professor Fuhui Wang is Associate Editor of npj Materials Degradation, but was not involved in the journal's review of, or decisions related to, this manuscript. The remaining authors declare no competing financial or non-financial interests. The other authors do not have a competing interest.

References

[1] Vahidshad, Y. & Khodabakhshi, A.H. An investigation of different parameters on the penetration depth and welding width of Ti-6Al-4V alloy by plasma arc welding. *Welding in the World* . **65**, 485-497; 10.1007/s40194-020-01024-9 (2020).

[2] Bendikiene, R. et al. Comparative study of TIG welded commercially pure titanium. *Journal of Manufacturing Processes.* **36**, 155-163; 10.1016/j.jmapro.2018.10.007 (2018).

[3] Schwab, S., Selin, R. & Voron, M. Welding materials for TIG welding, surfacing, and WAAM technology of titanium alloys. *Welding in the World*. **67**, 981-986; 10.1007/s40194-023-01464-z (2023).

[4] Kovačócy, P. et al. Investigation of the Microstructure and Mechanical Characteristics of Disk

Laser-Welded Ti-6Al-4V Alloy Joints. *J. Mater. Eng. Perform.* **29**, 593-606; 10.1007/s11665-019-04539-5 (2020).

[5] Bhattacharyya, D. et al. The role of crystallographic and geometrical relationships between α and β phases in an α/β titanium alloy. *Acta Mater.* **51**, 4679-4691; 10.1016/s1359-6454(03)00179-4 (2003).

[6] Diao, Y. & Zhang, K. Microstructure and corrosion resistance of TC2 Ti alloy by laser cladding with Ti/TiC/TiB2 powders. *Appl. Surf. Sci.* **352**, 163-168; 10.1016/j.apsusc.2015.04.030 (2015).

[7] Han, Z., Zhao, H., Chen, X.F. & Lin, H.C. Corrosion behavior of Ti-6Al-4V alloy welded by scanning electron beam. *Mater. Sci. Eng. A*. **277**, 38-45; 10.1016/s0921-5093(99)00561-4 (2000).

[8] Wang, L.M. & Lin, H.C. The characterization of corrosion resistance in the Ti-6Al-4V alloy fusion zone using a gas tungsten arc welding process. *J. Mater. Res.* **24**, 3680-3688; 10.1557/jmr.2009.0444 (2009**)**.

[9] Atapour, M., Fathi, M.H. & Shamanian, M. Corrosion behavior of Ti–6Al–4V alloy weldment in hydrochloric acid. *Mater. Corros.* **63**, 134-139; 10.1002/maco.201005821 (2010**)**.

[10] Li, Z. et al. Microstructure and corrosion resistance of fusion zone in Ti-6Al-4V alloy welded using pulsed- and continuous-wave lasers. *Corros. Sci.* **220**, 111269; 10.1016/j.corsci.2023.111269 (2023**)**.

[11] Zhang, L., Wu Z., Li Y. & Zhao, F. Mechanical properties and corrosion resistance of TC4 titanium alloy joints by plasma arc welding + gas tungsten arc welding combination welding. *Journal of Materials Science*. **59**, 13234-13250; 10.1007/s10853-024-09967-w (2024).

[12] Zhang, H. et al. Stress corrosion behavior and mechanism of Ti6321 alloy with different

microstructures in stimulated deep-sea environment. *Corros. Sci.* **233**, 112059; 10.1016/j.corsci.2024.112059 (2024**)**.

[13] Gao, F. et al. Stress corrosion characteristics of electron beam welded titanium alloys joints in NaCl solution. *Mater. Charact.* **192**, 112126; 10.1016/j.matchar.2022.112126 (2022).

[14] Xiong, X.L. et al. Hydrostatic pressure effects on the kinetic parameters of hydrogen evolution and permeation in Armco iron. *Electrochim. Acta*. **255**, 230-238; 10.1016/j.electacta.2017.09.181 (2017).

[15] Sun, H., Liu, L., Li, Y. & Wang, F. Effect of Hydrostatic Pressure on the Corrosion Behavior of a Low Alloy Steel. *J. Electrochem. Soc.* **160**, C89-C96; 10.1149/2.040303jes (2013).

[16] Sun, H. et al. The performance of Al–Zn–In–Mg–Ti sacrificial anode in simulated deep water environment. *Corros. Sci.* **77**, 77-87; 10.1016/j.corsci.2013.07.029 (2013).

[17] Hu, S. et al. Influence of hydrostatic pressure on the corrosion behavior of 90/10 copper-nickel alloy tube under alternating dry and wet condition. *Corros. Sci.* **146**, 202-212; 10.1016/j.corsci.2018.10.036 (2019).

[18] Jin, Y. et al. Study on corrosion fatigue of Ti-6Al-4V alloy under hydrostatic pressure environment in 3.5 % NaCl solution. *Corros. Sci.* **252**, 112950; 10.1016/j.corsci.2025.112950 (2025**)**.

[19] Liu, R., Cui, Y., Liu, L. & Wang, F. Study on the mechanism of hydrostatic pressure promoting electrochemical corrosion of pure iron in 3.5% NaCl solution. *Acta Mater.* **203**, 116467; 10.1016/j.actamat.2020.11.009 (2021**)**.

[20] Ma, R. et al. Effect of hydrostatic pressure on the thermodynamic and kinetic behavior of

metal electrode reactions. *Electrochim. Acta*. **424**, 140617; 10.1016/j.electacta.2022.140617 (2022**).**

[21] Hu, S. et al. Effect of hydrostatic pressure on the galvanic corrosion of 90/10 Cu-Ni alloy coupled to Ti6Al4V alloy. *Corros. Sci.* **163**, 108242; 10.1016/j.corsci.2019.108242 (2020**)**.

[22] Liu, R. et al. Failure mechanism of Al-Zn-In sacrificial anode under the synergic action of water pressure and fluid in the extreme deep-sea environment. *Corrosion Communications*. **14**, 39-48; 10.1016/j.corcom.2023.07.002 (2024**).**

[23] Liu, R. et al. Stress corrosion cracking of the titanium alloys under hydrostatic pressure resulting from the degradation of passive films. *Acta Mater.* **252**, 118946; 10.1016/j.actamat.2023.118946 (2023**)**.

[24] Liu, R. et al. A primary study of the effect of hydrostatic pressure on stress corrosion cracking of Ti-6Al-4V alloy in 3.5% NaCl solution. *Corros. Sci.* **165**, 108402; 10.1016/j.corsci.2019.108402 (2020**)**.

[25] Liu, R. et al. Unveiling the effect of hydrostatic pressure on the passive films of the deformed titanium alloy. *Corros. Sci.* **190**, 109705; 10.1016/j.corsci.2021.109705 (2021**)**.

[26] Pan, Y. et al. Investigating the environmental factors on corrosion and stress corrosion cracking behavior of Ti-6Al-3Nb-2Zr-1Mo alloy in simulated seawater. *Corros. Sci.* **259**, 113487; 10.1016/j.corsci.2025.113487 (2026**)**.

[27] Pan, Y. et al. A comparative study on the passive film and SCC behavior of Ti-6Al-3Nb-2Zr-1Mo alloy at various test temperatures in simulated seawater. *Corros. Sci.* **233**, 112066; 10.1016/j.corsci.2024.112066 (2024**)**.

[28] ASTM G129, Standard Practice for Slow Strain Rate Testing to Evaluate the Susceptibility of Metallic Materials to Environmentally Assisted Cracking. West Conshohocken, PA 2013.

[29] Dong, Y. et al. Stress corrosion cracking of TC4 ELI alloy with different microstructure in 3.5% NaCl solution. *Mater. Charact.* **194**, 112357; 10.1016/j.matchar.2022.112357 (2022**)**.

[30] ASTM G30, Standard Practice for Making and Using U-Bend Stress-Corrosion Test Specimens, West Conshohocken, PA, 2009.

[31] Lu, H. et al. Tailoring microstructure of additively manufactured Ti6Al4V titanium alloy using hybrid additive manufacturing technology. *Additive Manufacturing*. **63**, 103416; 10.1016/j.addma.2023.103416 (2023**).**

[32] Zhang, J. et al. Corrosion behaviors of Zn/Al–Mn alloy composite coatings deposited on magnesium alloy AZ31B (Mg–Al–Zn), *Electrochim. Acta*. **55**, 560-571; 10.1016/j.electacta.2009.09.026 (2009**).**

[33] Hirschorn, B. et al. Determination of effective capacitance and film thickness from constant-phase-element parameters. *Electrochim. Acta*. **55**, 6218-6227; 10.1016/j.electacta.2009.10.065 (2010**)**.

[34] Ellerbrock, D. & Macdonald, D.D. Passivity of titanium, part 1: film growth model diagnostics. *J. Solid State Electrochem.* **18**, 1485-1493; 10.1007/s10008-013-2334-6 (2014).

[35] Roh, B. & Macdonald, D.D. Passivity of titanium: part II, the defect structure of the anodic oxide film. *J. Solid State Electrochem.* **23**, 1967-1979; 10.1007/s10008-019-04254-0 (2019**).**

[36] Macdonald, D.D. The Point-Defect Model for the Passive State. *J. Electrochem. Soc.* **139**, 3434-3449; 10.1149/1.2069096 (1992**)**.

[37] Kolman, D.G., Gaudettb, M.A. & Scully, J.R. Modeling of anodic current transients resulting from oxide rupture of plastically strained β + α titanium. *J. Electrochem. Soc.* **145**, 1829-1840; 10.1149/1.1838564 (1998**)**.

[38] Wanhill, R.J.H. Aqueous Stress Corrosion in Titanium Alloys. *Br. Corros. J.* **10**, 69-78; 10.1179/000705975798320783 (1975).

[39] Gao, K.W. et al. In-situ transmission electron microscopic observation of corrosion-enhanced dislocation emission and crack initiation of stress corrosion. *Corrosion*. **56**, 515-522; 10.5006/1.3280556 (2000).

[40] Ahmed, T. & Rack, H. J. Phase transformations during cooling in α+β titanium alloys. *Mater. Sci. Eng.A*. **242**, 206-211; 10.1016/s0921-5093(97)00802-2 (1998).

[41] Kumar, C., Das, M., Paul, C.P. & Bindra, K.S. In-situ transmission electron microscopic observation of corrosion-enhanced dislocation emission and crack initiation of stress corrosion. *Opt Laser Technol*. **105**, 306-321; 10.1016/j.optlastec.2018.02.021 (2018).

[42] Qin, Z. et al. Passive film-induced stress and mechanical properties of α-Ti in methanol solution. *Corros. Sci.* **78**, 287-292; 10.1016/j.corsci.2013.10.011 (2014**).**

Figures

Fig. 1 Stress-strain curves of Ti-6Al-4V for different welding regions.

Fig. 2 Mechanical properties of Ti-6Al-4V as determined by SSRT. (a) Yield strength, (b) ultimate tensile strength, (c) fracture elongation, and (d) stress corrosion cracking susceptibility.

Fig. 3 Fracture morphology of BM samples post SSRT. (a) In air, (b) in 3.5% NaCl solution at 0.1 MPa, and (c) in 3.5% NaCl solution at 15 MPa.

Fig. 4 Fracture morphology of HAZ samples post SSRT. (a) In air, (b) in 3.5% NaCl solution at 0.1 MPa, and (c) in 3.5% NaCl solution at 15 MPa.

Fig. 5 Fracture morphology of WM samples post SSRT. (a) In air, (b) in 3.5% NaCl solution at 0.1 MPa, and (c) in 3.5% NaCl solution at 15 MPa.

Fig. 6 Analysis of fractal dimension on dimple areas of tensile fracture surfaces of Ti-6Al-4V weld specimens under different environmental conditions.

Fig. 7 Orientation maps of different welding zones in Ti-6Al-4V. (a1, a2) Orientation maps in the x-direction and z-direction of the original BM samples, (b1, b2) orientation maps in the x-direction and z-direction of BM samples after SSRT to yield under 15 MPa, (c1, c2) orientation maps in the x-direction and z-direction of the original HAZ samples, (d1, d2) orientation maps in the x-direction and z-direction of HAZ samples after SSRT to yield under 15 MPa, (e1, e2) orientation maps in the x-direction and z-direction of the original WM samples, and (f1, f2) orientation maps in the x-direction and z-direction of WM samples after SSRT to yield under 15 MPa.

Fig. 8 IPF maps of different welding regions in Ti-6Al-4V. (a1) IPF map of the original BM samples, (a2) IPF map of BM samples after SSRT to yield under 15 MPa, (b1) IPF map of the original HAZ samples, (b2) IPF map of HAZ samples after SSRT to yield under 15 MPa, (c1) IPF map of the original WM samples, and (c2) IPF map of WM samples after SSRT to yield under 15 MPa.

Fig. 9 KAM and basal slip Schmid factor maps of different welding zones in Ti-6Al-4V. (a1) KAM map of the original BM samples, (a2, a3) KAM map and basal slip Schmid factor map of BM samples after SSRT to yield under 15 MPa, (b1) KAM map of the original HAZ samples, (b2, b3) KAM map and basal slip Schmid factor map of HAZ samples after SSRT to yield under 15 MPa, (c1) KAM map of the original WM samples, (c2, c3) KAM map and basal slip Schmid factor map of WM samples after SSRT to yield under 15 MPa, (d1) Distribution of original local misorientation across different welding zones, and (d2, d3) distribution of local misorientation and basal slip Schmid factor across different welding zones after SSRT to yield under 15 MPa.

Fig. 10 EIS results of different welding regions of Ti-6Al-4V. (a) Nyquist plot of BM samples in solution at 0.1 MPa, (b) Nyquist plot of HAZ samples in solution at 0.1 MPa, (c) Nyquist plot of WM samples in solution at 0.1 MPa, (d) Nyquist plot of BM samples in solution at 15 MPa, (e) Nyquist plot of HAZ samples in solution at 15 MPa, and (f) Nyquist plot of WM samples in solution at 15 MPa.

Fig. 11 Fitting results of electrochemical impedance of different welding regions. (a) Equivalent circuit, (b) variation pattern of fitting parameter R_1, and (c) variation pattern of fitting parameter $1/C_{\mathrm{eff},1}$.

Fig. 12 The schematic diagram of stress corrosion mechanism of Ti-6Al-4V alloy in different welding areas under 15 MPa hydrostatic pressure

Fig. 13 Schematic representation and microstructural analysis of titanium alloy welding. (a) Sampling diagram of a Ti-6Al-4V welded plate, (b) dimensions of tensile specimens, (c) CCT phase diagram of Ti-6Al-4V alloy, (d) metallographic microscope image of BM, (e) metallographic microscope image of HAZ, (f) metallographic microscope image of WM, (g) metallographic microscope image of HAZ adjacent to BM, and (h) metallographic microscope image of HAZ near WM.

Table

Table 1 TIG welding parameters for Ti-6Al-4V alloys.

Welding Parameters	Values
Welding current (A)	200
Welding voltage (V)	17
Welding speed (cm/min)	15
Plasma gas flow rate (lpm)	5
Torch position	Vertical